

2. INTRODUCTION

Scientific interest into aerodynamics of airfoils at low-medium Reynolds numbers (ca. 100,000 - 4,000,000) has gained popularity in recent years with their application to unmanned aircraft and urban air mobility vehicles (see [1]). The accurate prediction of an airfoil's aerodynamic characteristics is crucial in any development process, as it will significantly affect the performance of the overall vehicle. Modern airfoil design often requires a significant amount of numeric simulations to be performed in a highly automated manner. Similar challenges are found in large-scale numeric investigations of airfoils relevant in aerodynamic research or aircraft design. Such analyses were yet limited to panel methods with viscous formulations like XFOIL [2] or JavaFoil (based on [3]). The viscous formulations employ classic boundary layer theory and couple the results with a potential flow panel method. Transition is typically modeled with a spatial-amplification theory like the e^N method. Codes like XFOIL or Java Foil have seen extensive use in the past due to their high level of automation and fast calculation times. User input is minimal and restricted to providing airfoil shape coordinates and setting flow parameters. XFOIL was validated on multiple occasions (e.g. [4] and [5]) for predicting transition location and airfoil lift. However, it is frequently described to underpredict profile drag especially in the presence of laminar separation bubbles [6] or thick airfoils [7].

The simulation of low Reynolds number flows with Reynolds-Averaged Navier-Stokes (RANS) solvers has been considered challenging in the past, as most turbulence models essentially imply fully turbulent flow. The recent development of the γ - Re_{θ} [8] and successively γ [9] local correlation-based transition model has changed this point of view. Both transition models are coupled to the SST turbulence model [10] and have been extensively validated (see [11–13]). They are accurate in predicting laminar-turbulent transition location as well as lift and drag characteristics of airfoils at low Reynolds numbers.

Today's computational power allows performing a significant number of RANS airfoil simulations in acceptable time frames. However, the simulation setup of an airfoil analysis with a RANS-transition approach is much more complicated compared to panel methods like XFOIL. Usually, significant human interaction for geometry preparation, domain and mesh creation, setup of flow solver and post-processing is required. This makes RANS simulations unattractive considering the large quantities of airfoil simulations that are required in aerodynamic research or aircraft design.

To overcome this restriction, a highly automated airfoil analysis method applying 2D-RANS simulations is presented in this publication. Human interaction for the complete simulation setup is restricted to the specification of airfoil shape coordinates and flow properties. The manual effort for performing a complete RANS-transition simulation is therefore reduced to what is known from panel methods like XFOIL.

The process is suited for detailed airfoil aerodynamic research and implementation in multidisciplinary aircraft design environments. Both flow properties and airfoil shapes can be easily changed, which allows completely automating large-scale parametric studies. The novel approach makes use of both NASA's Open Vehicle Sketch Pad [14] for geometry creation and surface discretization and Siemens' StarCCM+ [15] for hybrid prism-polyhedral mesh creation and solution. StarCCM+ is very well validated (see [16–18]) and widely used in industry and academia. Transition is modeled with either the γ - Re_{θ} or γ model in combination with the SST model. StarCCM+ is chosen, as it is the respective CFD software used by FH Aachen. The outlined process, however, can easily be transferred to other CFD software like FLUENT or OpenFoam. The paper describes both the overall process and detailed physical settings, which were used to achieve the most promising compromise between automation, accuracy and time consumption. It is well suited for any airfoil shape and shows superior accuracy compared to XFOIL. Numerous validation cases are provided that include basic airfoils (NACA 0015), low Reynolds number airfoils (E387, FX05-188) and natural laminar flow airfoils (NLF(1)-1015).

3. NOVEL SIMULATION PROCESS

The novel method combines existing geometry creation and numerical simulation software in an innovative way. Third-party software products that are used in the novel procedure are not modified themselves. However, the individual procedures that usually require human interaction are highly automated via the use of scripts and macro files. This allows to perform all necessary steps in the simulation setup fully automatic. A schematic overview of the novel simulation process is shown in Fig. 3.1.

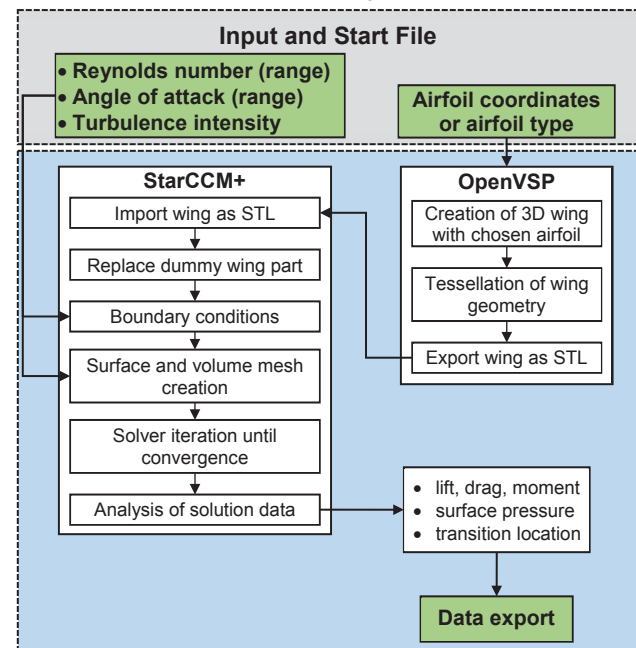


Fig. 3.1 Schematic of simulation process

The user inputs the desired Reynolds number, turbulence intensity, and angle of attack for the simulation in a text file. It is also possible to enter both a range of angles of attack and Reynolds numbers. Necessary parts of the process are then performed consecutively. Airfoils can be specified in standard ASCII text format as a series of (x,y) coordinate pairs. It is possible to sequentially analyze multiple airfoils one after another. This allows performing full factorial design studies based on Reynolds number, angle of attack and airfoil geometry.

A script for OpenVSP automatically creates a 3D wing that is tessellated and exported as a Stereolithography file (STL). Another script starts a predefined StarCCM+ simulation file and exchanges the newly created wing STL file with a dummy file in the simulation. The surface and volume meshing operations are always linked to this dummy wing file. The 3D geometry is then transferred into a 2D domain. Another script transfers the user input Reynolds number and angle of attack to predefined parameters in StarCCM+. These parameters are used to adjust surface and volume mesh operations based on their values. Reynolds number and angle of attack also adjust both inflow and outflow boundary conditions.

The solver is started after the mesh is created and runs until some convergence criteria are satisfied. Forces and moments of the airfoil are evaluated after convergence and exported in ".csv" format. Further exports include a pressure coefficient distribution and the local skin friction coefficient that allows determining the transition location. The following sections give details of the individual parts of the novel simulation process and highlight essential settings.

3.1. OpenVSP: Wing creation and tessellation

OpenVSP is a software tool that was originally created for conceptual aircraft design. It allows to quickly generate a complete aircraft geometry by modifying predefined parts (e.g. wing or fuselage). The novel process uses the wing-modeling tool of OpenVSP to create a straight 3D wing of chord length 1 m and span 1 m. No twist, dihedral or taper is used. The creation of a 3D body is necessary, as most CFD software only allows 3D parts to be imported, even though a 2D analysis is later performed. Fig. 3.2a shows the 3D wing automatically created in OpenVSP. The airfoil to be analyzed is assigned to the root and tip of the wing. Airfoils are universally specified as a series of x and y coordinates in an ASCII file. The well-known Selig ".dat" format is preferred. Other formats are possible as long as OpenVSP can interpret them (see [19]). The airfoils' circumference is discretized by 800 points, whereby points are locally clustered at leading and trailing edge. 800 points are far more than what is usually supplied by airfoil input files and achieved via interpolation. The surface discretization is shown in Fig. 3.2b on a side-view.

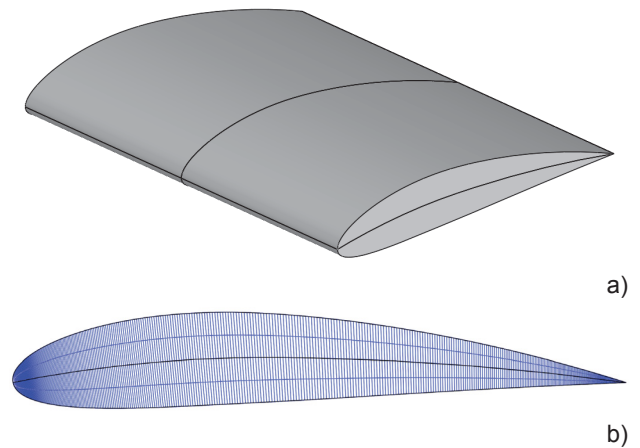


Fig. 3.2 a) wing surface in OpenVSP, b) side-view of STL tessellation of wing

A fine discretization is desirable in two ways: First, it guarantees that any airfoil shape can be appropriately captured. This is especially critical for thin airfoils with small leading edge radii. Second, the OpenVSP discretization is essentially finer than the discretization later created in the CFD software. This is beneficial, as several meshing algorithms require a high-quality input surface as they rely on it for volume meshing. Discretization in spanwise direction is of minor importance as only a 2D mesh is created. OpenVSP can also directly specify airfoils that are governed by certain spline functions like NACA 4 or NACA 5 series. These airfoils do not require a file input but rather the specification of their design parameters. The novel workflow currently allows this automated option for NACA 4 series airfoils.

The geometry is exported in vendor-neutral stereolithography file format, which directly uses the surface discretization of OpenVSP. The surface is represented by small flat triangles. Curvature is captured by a reduction in triangle size.

3.2. StarCCM+: Simulation setup

A universal StarCCM+ simulation file is designed and re-used for each simulation. It contains the complete physical simulation setup and all necessary parameters to create an adequate mesh and solve the governing equations. The simulation setup is designed as a pipeline of consecutive tasks in order to set up the overall simulation (compare Fig. 3.1). A change in one of these tasks requires the re-execution of all following tasks.

In a first step, an external macro imports the user-specified Reynolds number (range), turbulence intensity and angle of attack (range) into the universal simulation file. The variables are stored as internal parameters and can then be used to manipulate settings of the simulation.

A completely automated simulation requires the pre-definition of multiple aspects (e.g. domain settings, boundary conditions, mesh settings). The following sections describe these aspects in detail and present any assumptions made.

3.2.1. Flow field and boundaries

The computational domain is bullet-shaped, extends 300 airfoil chord lengths and follows recommendations from [20]. It is shown in Fig. 3.3, whereby the airfoil is much enlarged to make it visible. The domain body is created through subtracting a flow field body (dashed line in Fig. 3.3) and a dummy wing body (dash-dotted line in Fig. 3.3). The resulting body is transferred into 2D. Each time a new airfoil should be analyzed, the surface of the dummy wing body is replaced with the imported STL surface file from OpenVSP. This process is automated with a macro. Replacing the dummy wing's surface introduces a change at the beginning of the simulation pipeline and requires the re-execution of all following tasks.

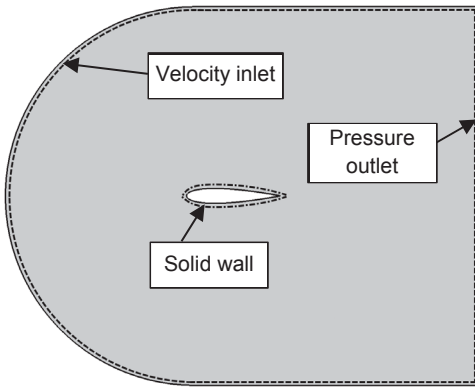


Fig. 3.3 Computational domain and boundaries (not to scale)

The three boundaries used in the computational model are highlighted in Fig. 3.3. Boundary conditions and solver are designed to handle incompressible as well as mildly compressible cases (maximum inflow $Ma \approx 0.5$). Table 1 gives an overview about the physical reference parameter used in the simulation.

Table 1 physical reference parameter

Reference parameter	
pressure	101325 Pa
density	1.225 kg/m ³
viscosity	1.81205 x 10 ⁻⁵ Pa s
temperature	288.15 K
chord length	1 m
ideal gas constant	287.1 J/kgK
isentropic exponent	1.4

The magnitude of the inflow velocity is computed from the user input Reynolds number and split into vector components via the specified angle of attack (see Eq. (1-2)).

$$u_{ref} = \frac{Re \cdot \mu_{ref}}{c_{ref} \cdot \rho_{ref}} \quad (1)$$

$$\vec{u} = u_{ref} \cdot \begin{pmatrix} \cos AoA \\ \sin AoA \end{pmatrix} \quad (2)$$

The static temperature at the inlet boundary is kept constant while static pressure is extrapolated from within the interior of the domain. Density is calculated through the ideal gas equation. The pressure outlet boundary assumes the environmental reference pressure and calculates the outflow velocity based on an extrapolation from the adjacent cell. The static reference temperature is again fixed and density calculated as for the inflow boundary. The airfoil's surface is treated as an adiabatic no-slip wall that enforces zero velocity on the surface.

Transport variables for the turbulence model at inlet and outlet are specified as turbulence intensity and an eddy viscosity ratio. Turbulence intensity is user-specified and taken from the input file. Experiments indicate that turbulence intensities of less than 0.1% have no significant effect on the transition location anymore [21]. A value of 0.08% is specified as the default value in case the user does not specify a turbulence intensity (see Spalart and Rumsey [22]). The eddy viscosity ratio is fixed at 1.0 in compliance with recommendations found in [9]. Turbulence intensity and eddy viscosity ratio are transferred to the transported variables of the SST model via Eq. (3-4).

$$k = \frac{3}{2} ((T. i.) \cdot u_{ref})^2 \quad (3)$$

$$\omega = \frac{\rho \cdot k}{\left(\frac{\mu_r}{\mu_{ref}}\right) \mu_{ref}} \quad (4)$$

The physical approach implies that an increase in freestream Reynolds number also increases the freestream Mach number. A freestream Reynolds number of 7 million leads to a freestream Mach number of 0.3. Up to this Mach number, compressibility effects are of minor importance in airfoil aerodynamics [23]. The current simulation process is therefore limited to this Reynolds number. Higher Reynolds numbers can be conveniently implemented by increasing the airfoil's chord length without affecting Mach number. This, in turn, requires adjustments to all settings that are affected by chord length and is currently not fully automated.

3.2.2. Mesh generation

The computational domain is discretized with an unstructured hybrid prism-polyhedral mesh. The mesh creation is part of the simulation pipeline and uses the integrated meshing algorithm provided by StarCCM+.

Polyhedral cells are advantageous as they have more neighboring cells compared to hexahedral or tetrahedral ones. Information, therefore, spreads faster through the domain leading to faster convergence [24]. This is especially helpful in low Reynolds number cases, where the freestream flow velocity is small. These cases were observed to require high numbers of iterations to achieve convergence. This can be roughly attributed to the slow numerical information transfer that is somewhat proportional to the flow speed.

The prism layer mesh discretizes the near-wall region to sufficiently resolve gradients in the boundary layer. RANS transition simulations with the γ - Re_{θ} - or γ model require a very fine boundary layer discretization. The near-wall mesh settings follow recommendations presented by Menter et al. [9]. The process uses 40 layers of prismatic cells in the wall-normal direction. The layering follows a hyperbolic tangent approach introduced in [25] (see Eq. (5))

$$y(n_i) = 1 + \frac{\tanh\left(s\left(\frac{n_i}{N_t}-1\right)\right)}{\tanh(s)} \quad (5)$$

Eq. (5) takes values from zero to one, depending on the layer number n_i . N_t is the total number of prism layers. S is a stretching factor and set to 1.5. Eq. (5) is multiplied with the local prism layer thickness. This computes the wall distance of the respective cell layer and leads to the distribution shown in Fig. 3.4a. The first cell height is estimated with Eq. (6-8) (adapted from [26]), whereby y^+ is set to 0.2 in Eq. (8). Extensive testing has shown that this guarantees y^+ values in the converged solution that are consistently smaller than 0.5 for all surface cells.

$$C_f = (2 \cdot \log_{10}(Re) - 0.65)^{-2.3} \quad (6)$$

$$\tau_w = \frac{C_f \rho \left(\frac{Re \cdot \mu_{ref}}{\rho_{ref} \cdot c_{ref}}\right)^2}{2} \quad (7)$$

$$\Delta s = \frac{y^+ \mu}{\sqrt{\frac{\tau_w}{\rho}}} \quad (8)$$

The thickness of the prism layer mesh is calculated by estimating the height of a fully turbulent boundary layer at the trailing edge (see Eq. (9) adapted from [26]). This equation generally over predicts total boundary layer thickness as it assumes fully turbulent flow. However, an integrated algorithm ensures that the total prism layer thickness is smaller. It is adjusted to the local volume cell size, in order to guarantee a smooth transition between prism layer- and volume mesh (see Fig. 3.4a).

$$\delta = \frac{0.37 \cdot c_{ref}}{Re^{1/5}} \quad (9)$$

A change in Reynolds number automatically adapts prism layer thickness as well as first cell height through Eq. (6-9). It, therefore, requires a re-creation of the mesh.

The surface cell size is fixed to 0.4% of the chord length with an additional refinement at the leading edge (see Fig. 3.4b). This typically leads to around 600 cells discretizing the airfoil. Such fine mesh resolution is required to accurately capture transition effects at low Reynolds numbers [9]. The appropriate surface cell size was determined by extensive testing of a variety of airfoils. It is a compromise between accuracy and computational effort.

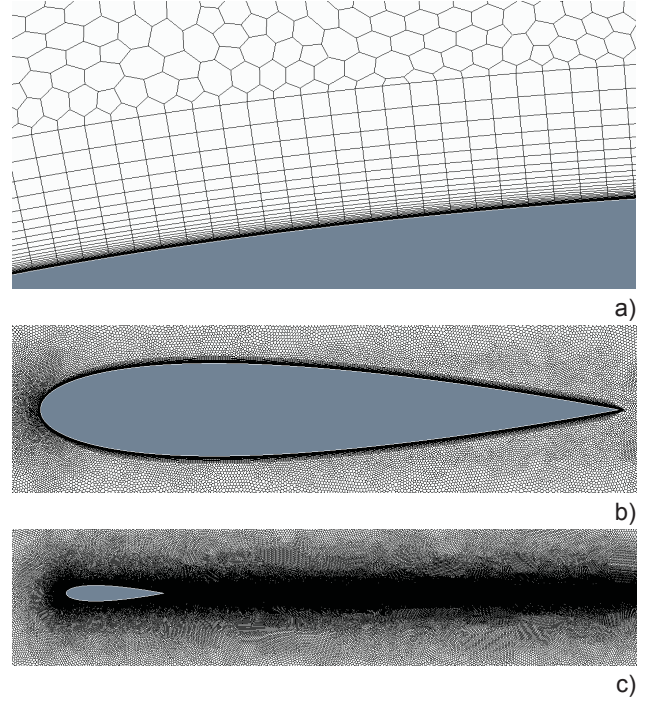


Fig. 3.4 Computational mesh: a) close-up of prism layers, b) near the airfoil, c) close-up wake refinement

The airfoil's wake is significantly refined for 20 chord lengths in order to capture fluctuations especially relevant in cases with flow separation. Cell sizes in this refinement area are in the order of the surface mesh. The length of the wake refinement region was evaluated by multiple tests. The direction of the wake refinement is adjusted for the inflow angle of attack.

The overall cell count in the simulations is usually between 320,000 and 400,000 depending on the airfoil. The final mesh settings were evaluated by testing the settings for a variety of airfoil shapes and Reynolds numbers. The results of one mesh independence study are exemplarily shown in Fig. 3.5. The cell count is here increased by globally decreasing the size of all cells simultaneously. All analyzed parameters stagnate using more than 250,000 cells.

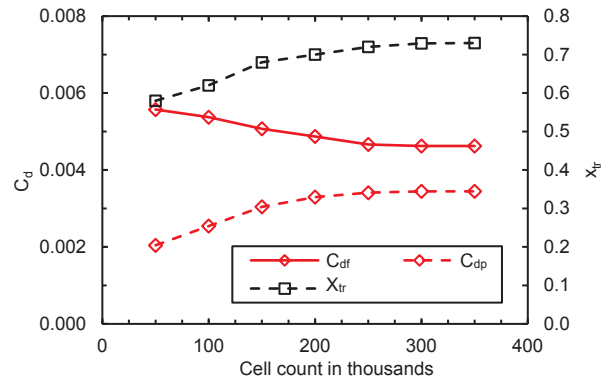


Fig. 3.5 Mesh independence study for NACA 0016 at $Re=500,000$ based on friction drag, pressure drag and transition location.

3.2.3. Turbulence and transition model

Turbulence is simulated with Menter's SST model [10] that effectively combines the advantageous of a k - ϵ formulation in the far-field with a k - ω formulation close to walls. The SST model is widely used for aerodynamic simulations (see [16, 27, 28]) and was validated multiple times. The modeled eddy viscosity is transferred via a cubic non-linear constitutive relation into the fluctuating stress tensor. This was proposed by Hellsten [29] and derived as an explicit algebraic Reynolds stress model. It greatly enhances the prediction accuracy of anisotropy of turbulence.

Both γ - Re_θ and γ transition model use the concept of intermittency. The intermittency is an indicator of the state of the boundary layer. A purely laminar boundary layer has an intermittency of 0, while a fully turbulent one has 1. Values in between indicate transitional flow [21]. The γ - Re_θ and γ transition model incorporate a transport equation for the intermittency. The intermittency formulation triggers transition and is coupled to the SST turbulence model. It turns on the production term for the turbulent kinetic energy downstream of the transition location. The intermittency transport equation of the γ - Re_θ model is shown in Eq. (10). This form is not changed in the γ model.

$$\frac{\partial(\rho\gamma)}{\partial t} + \frac{\partial(\rho U_i \gamma)}{\partial x_i} = P_{\gamma 1} - E_{\gamma 1} + P_{\gamma 2} - E_{\gamma 2} + \frac{\partial}{\partial x_i} \left[\left(\mu + \frac{\mu_t}{\sigma_f} \right) \frac{\partial \gamma}{\partial x_i} \right] \quad (10)$$

$P_{\gamma 1}$ and $E_{\gamma 1}$ are transition sources that include an onset function to trigger the intermittency production. $P_{\gamma 2}$ and $E_{\gamma 2}$ are destruction sources and enable the model to predict re-laminarization. The onset function in the transition sources depends on the local vorticity Reynolds number and the critical momentum thickness Reynolds number $Re_{\theta c}$, where intermittency first increases in the boundary layer. The critical momentum thickness Reynolds number is connected to the transition onset momentum thickness Reynolds number $Re_{\theta t}$ via some empirical correlation. $Re_{\theta t}$ again depends on local freestream values of turbulence intensity and pressure gradient. Menter presents empirical correlations that link turbulence intensity and a pressure gradient parameter to the transition onset momentum thickness Reynolds number in the freestream. The freestream $Re_{\theta t}$ is then diffused into the boundary layer with a transport equation:

$$\frac{\partial(\rho \hat{Re}_{\theta t})}{\partial t} + \frac{\partial(\rho U_i \hat{Re}_{\theta t})}{\partial x_i} = P_{\theta t} + \frac{\partial}{\partial x_i} \left[\sigma_{\theta t} (\mu + \mu_t) \frac{\partial \hat{Re}_{\theta t}}{\partial x_i} \right] \quad (11)$$

$P_{\theta t}$ is a source term that ensures the transported scalar $\hat{Re}_{\theta t}$ follows the local freestream value of $Re_{\theta t}$ outside the boundary layer. $P_{\theta t}$ is turned off inside the boundary layer via some blending function. It effectively diffuses the freestream transition onset momentum thickness Reynolds number into the boundary layer as $\hat{Re}_{\theta t}$.

The γ transition model avoids a second transport equation, as turbulence intensity and pressure gradient parameter inside the boundary layer are approximated based on their freestream values. For details refer to Ref. [9].

Both γ - Re_θ and γ transition model are coupled to the SST model in the following way:

$$\frac{\partial(\rho k)}{\partial t} + \frac{\partial(\rho U_i k)}{\partial x_i} = \hat{P}_k - \hat{D}_k + \frac{\partial}{\partial x_i} \left[(\mu + \sigma_k \mu_t) \frac{\partial k}{\partial x_i} \right] \quad (12)$$

$$\frac{\partial(\rho \omega)}{\partial t} + \frac{\partial(\rho U_i \omega)}{\partial x_i} = \alpha \frac{P_k}{\nu_t} - D_\omega + C d_\omega + \frac{\partial}{\partial x_j} \left[(\mu + \sigma_k \mu_t) \frac{\partial \omega}{\partial x_j} \right] \quad (13)$$

$$\hat{P}_k = \gamma_{eff} P_k \quad (14)$$

$$\hat{D}_k = \min(\max(\gamma_{eff}, 0.1), 1.0) D_k \quad (15)$$

P_k and D_k are the production and destruction terms from the standard SST model. γ_{eff} is the effective intermittency that is obtained by correcting γ from Eq. (10) for separation induced transition effects (see [8]). Both Eq. (14) and Eq. (15) directly show how the intermittency triggers production or destruction terms for turbulent kinetic energy.

Multiple airfoil test simulations using either the γ - Re_θ and γ transition model yield very close results. Typically, the simulated drag force differs by a maximum order of 1.5% for a variety of airfoils that were tested. Lift force is near to identical. The deviations in drag can be attributed to a slightly different prediction of the turbulent transition behavior. Fig. 3.6 shows the skin friction coefficient of a NACA 0016 at $Re=1,400,000$ and 0° angle of attack, computed with γ - Re_θ and γ transition model. In this example, the skin friction coefficient simulated with both models is very similar, except near the turbulent reattachment location. The γ - Re_θ model shows a steeper gradient of the skin friction coefficient compared to the γ model. Additionally, the onset of turbulent reattachment is slightly more aft.

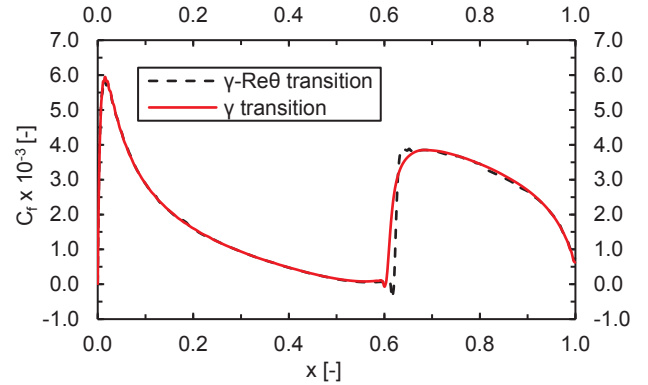


Fig. 3.6 Skin friction coefficient for NACA0016 at $Re=1,400,000$ and 0° angle of attack, computed with γ - Re_θ and γ -transition model

Within the novel simulation procedure, the transition location is determined from the course of the skin friction coefficient. In case a laminar separation is present, transition is assumed to be the point at which the skin friction coefficient achieves a positive value after being negative in the laminar

separation bubble. In case no separation occurs, transition is assumed where the skin friction coefficient has the highest gradient after reaching its minimum. Differences in skin friction calculation between γ - Re_{θ} and γ -transition model might lead to a deviation of transition location in a maximum order of 3% chord length.

The γ - Re_{θ} transition model is enabled by default. If desired, one can easily switch to the γ -transition model within the predefined simulation file.

3.2.4. Numerical solution and export

The solution algorithm uses a second-order upwind scheme for discretizing convective fluxes and central differences for diffusive fluxes. Cell center values and face gradients are computed with a Hybrid Gauss Least Squares Method. The pressure-based SIMPLE (Semi Implicit Method for Pressure Linked Equations) algorithm is employed to solve the Navier-Stokes equations in the steady-state RANS formulation. A more detailed description of this method can be found in Ref. [30].

Solution convergence is judged by monitoring lift, friction drag, pressure drag and pitching moment individually. The solution is stopped when all computed values do not change more than 0.05% for 2000 iterations. This typically leads to overall iteration counts between 15,000-50,000, very much depending on Reynolds number and associated flow speed. Flows governed by natural transition especially involving laminar separation bubbles at moderate angle of attack, might behave slightly unsteady. Such unsteadiness can be well observed by small fluctuations of pressure drag in the current approach. Within the converged case, pressure drag can slightly fluctuate around a constant mean value. Multiple tests confirmed that in such cases, the mean value of pressure drag in steady simulations is accurate when compared to time resolved simulations. The steady approach is therefore chosen as default. The user might switch to an unsteady solver if desired (high angle of attack, large separation) and can adjust the convergence criteria accordingly.

Airfoil forces are calculated by a discrete integration of both pressure and shear stresses on each surface cell of the airfoil (Eq. (16)). Pressure force acting on one surface cell is computed as the difference between acting pressure and reference pressure multiplied by the cell's face area vector (Eq. (17)). Friction is computed by multiplying the shear stress tensor with the cell face area vector (Eq. (18)). The integrated force is multiplied by a direction vector that depends on the angle of attack. Drag is measured in flow direction and lift perpendicular. Airfoil moment is computed in a similar manner by multiplying shear and pressure force on one surface cell with the respective cell's distance vector to the reference point. Moment reference point is taken as quarter chord.

$$Force = \sum_{fa} (f_{fa}^{pressure} + f_{fa}^{shear}) \quad (16)$$

$$f_{fa}^{pressure} = (p_{fa} - p_{ref}) \cdot a_{fa} \quad (17)$$

$$f_{fa}^{shear} = -T_{fa} \cdot a_{fa} \quad (18)$$

Forces and moments are normalized via the dynamic pressure and a reference area of 1 m² (1 m reference chord for moment coefficient). Lift coefficient, friction and pressure drag coefficients as well as pressure coefficient- and skin friction coefficient distribution are exported in ".csv" format.

4. EXAMPLES AND VALIDATIONS CASES

The following section provides a series of validation cases that were run to analyze the accuracy of the novel simulation procedure. The analysis of each airfoil only required the specification of the airfoil shape, Reynolds number (range), angle of attack (range) and turbulence intensity. The process is started and no further manual effort was necessary. The results with the novel procedure are compared to wind tunnel investigations found in the relevant literature. (see Table 2). The airfoils are intentionally chosen to follow different design philosophies in order to provide a wide variety of individual scenarios. The flow properties are adjusted to those found in the description of the wind tunnel investigations.

Table 2 Validation cases

Airfoil	Re x10 ⁶	T. i.	Reference
E387	0.2 - 0.46	<0.1%	Selig et al. [31]
SM701	1.0	<0.05%	Althaus et al. [6]
FX05-188	1.0 - 1.8	<0.02%	Wortmann [32]
NLF 10-15	0.5 - 1.0	<0.04%	Evangelista et al. [33]
NACA 0015	0.68	<0.08%	Sheldahl et al. [34]

4.1. Eppler 387

The Eppler 387 low Reynolds number airfoil (see Fig. 4.1) has been intensely studied in different wind tunnels and with numeric methods (e.g. [31, 35]). It has become a standard test case for the evaluation of novel computer codes.

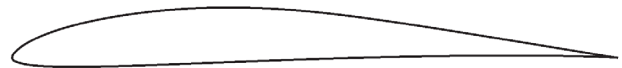


Fig. 4.1 E387 airfoil, max. $t/c=9.1\%$, max. camber= 3.2%

A comparison of simulated and measured data of the E387 airfoil is given in the following Fig. 4.2 to Fig. 4.6 .

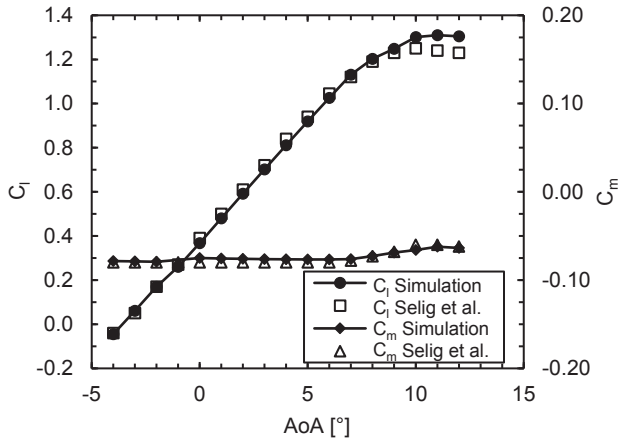


Fig. 4.2 Lift and moment coefficient of E387 at Re=460,000 with experimental data from [31]

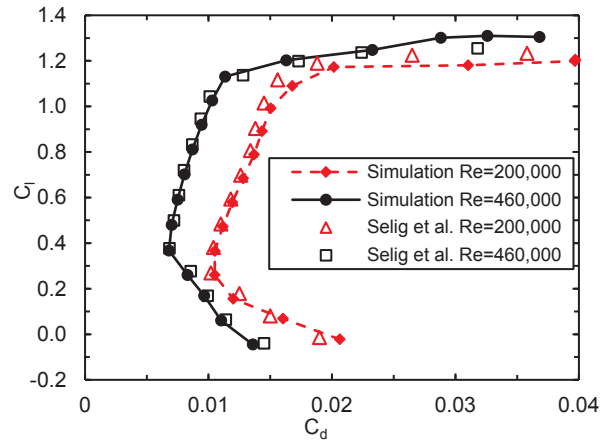


Fig. 4.3 Drag polars of E387 with experimental data from [31]

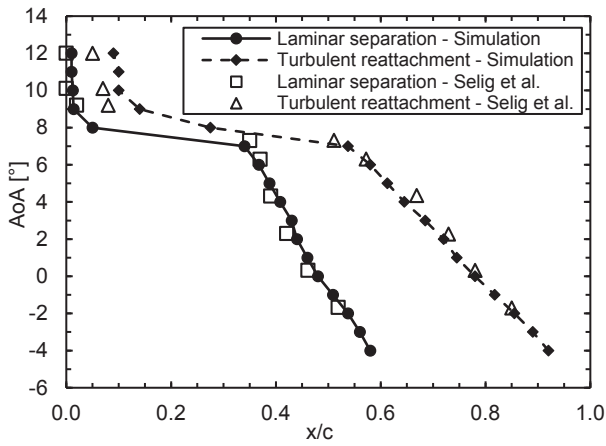


Fig. 4.4 Laminar separation and turbulent reattachment locations of E387 at Re=200,000 with experimental data from [4]

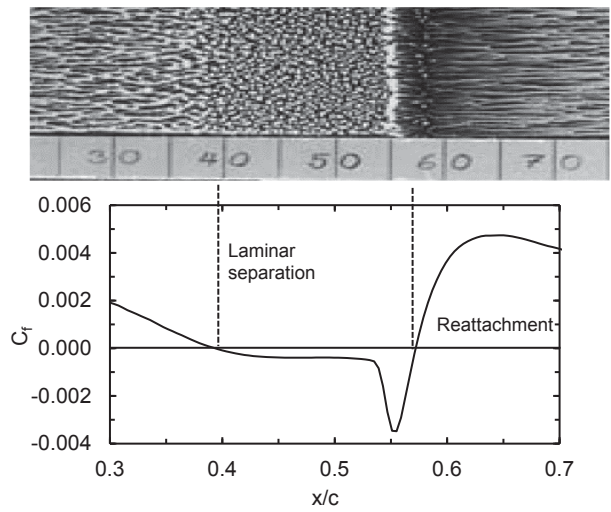


Fig. 4.5 Oil film image of transition region on E387 at Re=300,000 and 5° angle of attack and simulated course of skin friction coefficient. Oil film image reprinted with permission from [31]

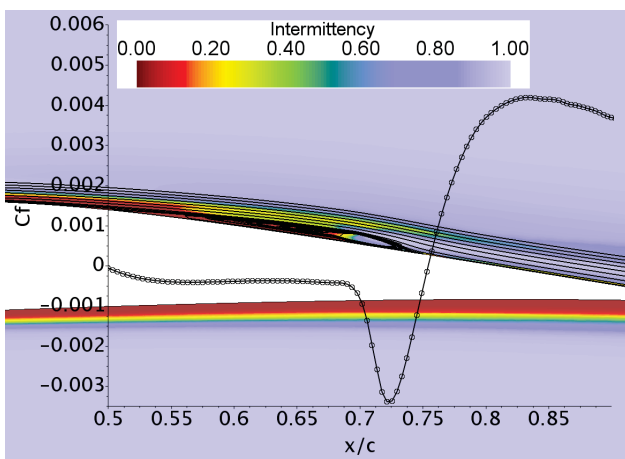


Fig. 4.6 Streamlines on top surface of E387 airfoil with local skin friction coefficient and intermittency at Re=200,000 and 0° angle of attack

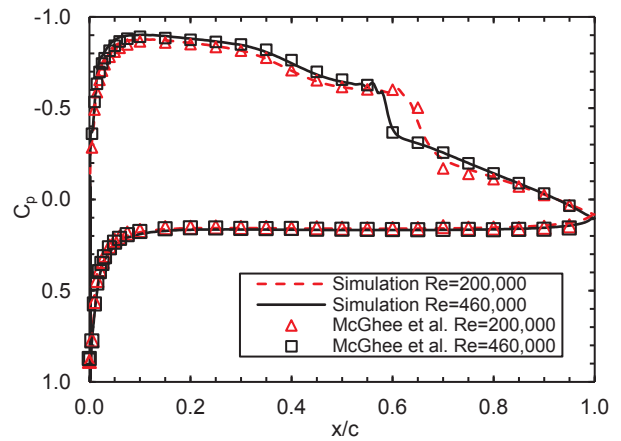


Fig. 4.7 Pressure coefficient of E387 at 3° angle of attack with experimental data from [35]

Simulated and measured lift and moment data of the airfoil at a Reynolds number of 460,000 are shown in Fig. 4.2. Both numeric and experimental values agree. Maximum lift is slightly overpredicted by about 4% and the angle for maximum lift is roughly a degree higher in the numeric simulation. A slight overprediction of maximum lift was noted on several occasions and is associated with a too late separation prediction by the turbulence model.

The drag polar of the airfoil at two Reynolds numbers is shown in Fig. 4.3. Numeric simulation and experiment match with deviations being below 3% for $C_l < 1$. Higher deviations are found at high-lift conditions for which drag values are affected by large separation areas.

The E387 in the low Reynolds number regime features a prominent laminar separation bubble. The laminar separation bubble is responsible for a large amount of the airfoil's total drag. It must be accurately modeled by the numeric approach in order to capture its effects. Fig. 4.4, therefore, shows a comparison of the location of laminar separation and turbulent reattachment of the E387 airfoil at $Re=200,000$. The experimental values are found by means of oil film technique, while numeric ones are determined from the local skin friction coefficient. Experimental and numeric data show good comparison up to 8° angle of attack. Both separation and reattachment location are sharply shifted forward in high-lift condition, which is well captured by the simulation. However, the simulation shows a turbulent reattachment location that is about 5% of the chord length more aft than measured in the wind tunnel. This correlates to an increased drag compared to wind tunnel data also evident in Fig. 4.3. With the bubble becoming very short, accurate measurement of the separation and attachment location with oil film technique gets complicated. The deviations between experiment and numerical simulation might, therefore also have their origin in measurement inaccuracies.

The skin friction coefficient is well suited to identify the start and end of separation bubbles as shown in Fig. 4.5. This figure compares the visual identification of transition effects

4.2. Somers Maughmer 701

The SM701 (see Fig. 4.8) was designed as a sailplane airfoil and investigated by several researchers in different wind tunnels (see [6, 36]).



Fig. 4.8 SM701 airfoil, max. $t/c=16.0\%$, max. camber= 3.0%

Lift and moment data simulated with the novel procedure are compared to experimental values and an XFOIL analysis ($N=9$) in Fig. 4.9. The novel approach simulates lift and moment of the airfoil very close to wind tunnel results.

using oil film technique with the course of the skin friction coefficient as simulated with the novel approach. The oil film image shows flow separation at about 40% chord length, which goes along with the skin friction coefficient becoming negative. Turbulent reattachment takes place at about 60% chord length, where the skin friction coefficient becomes positive again. Shortly before that, oil is accumulated at about 55% chord length. This is represented by the negative spike in skin friction coefficient and also described by Selig [31].

Oil accumulation and negative spike in skin friction coefficient are associated with a strong flow circulation zone shortly before turbulent reattachment takes place. The process can be identified in Fig. 4.6, according to the streamlines on the upper surface. This figure also shows the intermittency that is used to trigger the transition process. The intermittency increases sharply within the strong recirculation zone and triggers the production of turbulent kinetic energy in the SST model. The freestream flow around the airfoil has an intermittency of 1.0 and is treated as turbulent, as the $\gamma-Re_{\theta}$ model is a wall-bounded transition model.

A comparison of measured and simulated pressure coefficients on the airfoil's surface is shown in Fig. 4.7. Transition is evident through the pressure jump at about 60% and 65% chord length, respectively. The simulated pressure coefficient matches the experimental values and accurately represents the pressure jump associated with the transition process.

XFOIL is able to produce adequate data as well, however, more significant deviations are found for the moment coefficient.

The simulated airfoil's drag polar is shown in Fig. 4.10 together with experimental data and an XFOIL analysis. Drag simulated with the novel approach is very close to wind tunnel data with deviations on the order of 4% for moderate lift. Both the extent of the laminar bucket at low lift conditions, as well as drag at high-lift conditions match wind tunnel data. XFOIL, however, significantly under predicts total drag, while the extent of the laminar bucket is approximately comparable. At moderate lift conditions, the XFOIL drag values are between 13% and 18% lower than compared to wind tunnel data. This behavior was also noted by Althaus and Wurz [6] and a similar one found by Ramanujam et al. [7]. Further analysis has shown that XFOIL gives

much lower pressure drag values than compared to the novel simulation procedure. Friction drag, on the other hand, is very close. No further attempt is made to analyze

the origin of the deviations found for XFOIL as this is beyond the scope of this paper.

The novel simulation approach shows a higher level of accuracy than compared to XFOIL.

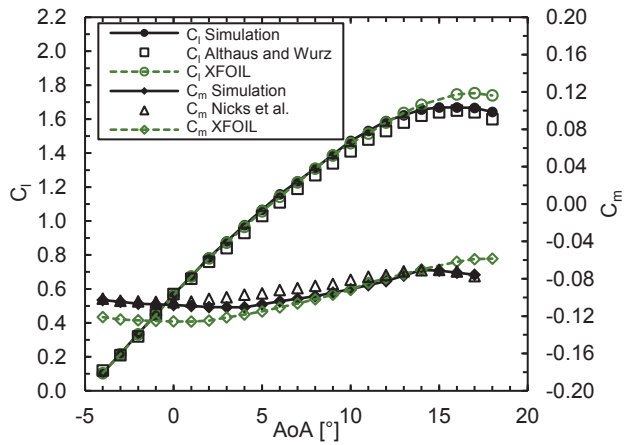


Fig. 4.9 Lift and moment coefficient of SM701 airfoil at Re=1,000,000 with experimental data from [6].

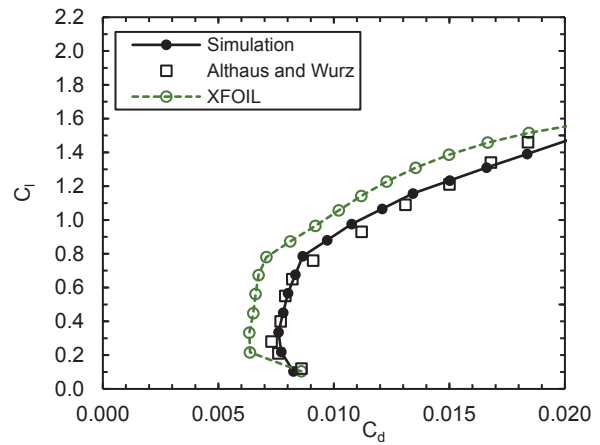


Fig. 4.10 Drag polar of SM701 airfoil at Re=1,000,000 with experimental data from [6].

4.3. Wortmann FX05-188

The Wortmann FX05-188 airfoil is intended as a natural laminar flow airfoil for sailplanes and helicopters. It is designed for a Reynolds number range between 0.5 - 3.0 million. The airfoil's shape is shown in Fig. 4.11 while Fig. 4.12 to Fig. 4.14 compare simulated data with available wind tunnel studies.

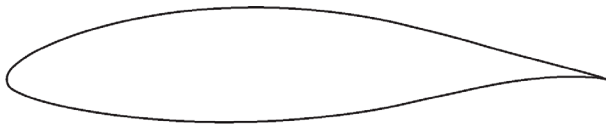


Fig. 4.11 FX05-188 airfoil, max. t/c=18.8%, max. camber=2.6%

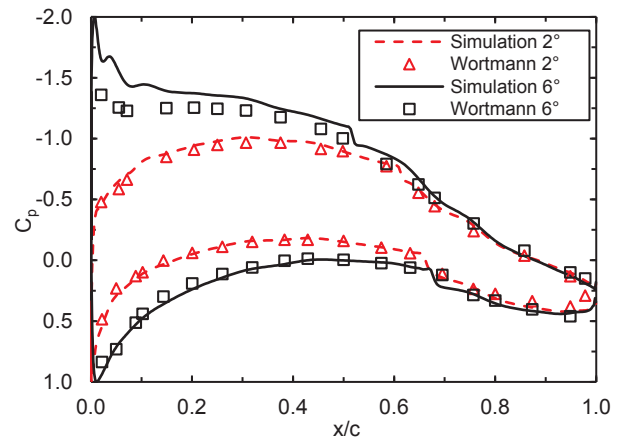


Fig. 4.13 Pressure coefficient of FX05-188 at Reynolds number 1,500,000 with experimental data from [32]

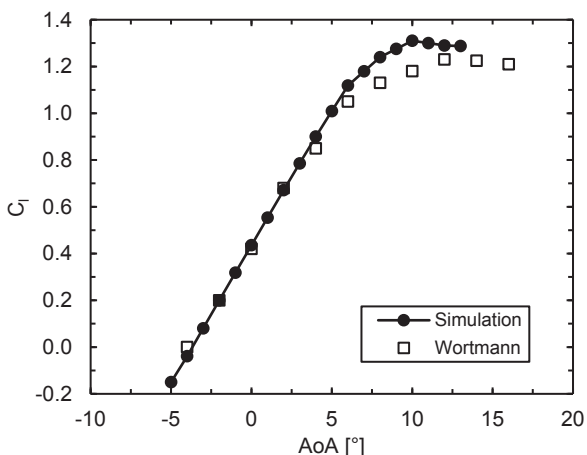


Fig. 4.12 Lift coefficient of FX05-188 airfoil at Re=1,500,000 with experimental data from [32]

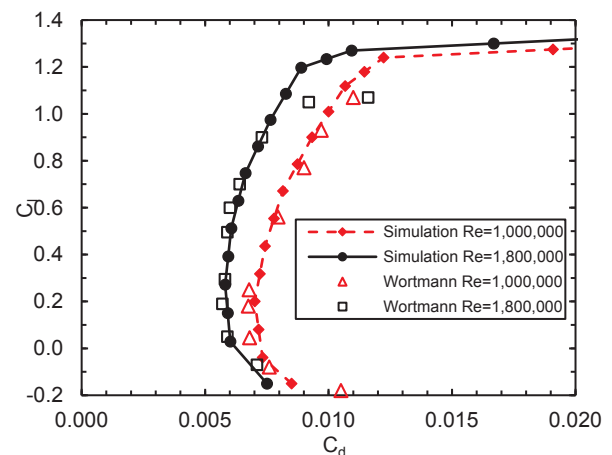


Fig. 4.14 Drag polars of FX05-188 airfoil with experimental data from [32]

The airfoil's lift-curve slope simulated with the novel approach matches the one found by experiments from Wortmann [32]. However, simulated lift at higher angles of attack differs from what is found in the experiment. The simulation predicts a higher maximum lift coefficient at a smaller angle of attack.

The cited airfoil lift from Wortmann was measured in the laminar wind tunnel of the University of Stuttgart. Wortmann states that due to the dimensions of the wind tunnel test section, maximum lift is measured with high uncertainty and typically too small. This is evident comparing measurements of NACA 6-series airfoils in the University of Stuttgart's wind tunnel with measurements taken in the NACA low turbulence tunnel [32]. Deviations between simulation and measurement at high-lift conditions must therefore also be attributed to measurement inaccuracies. The deviations found for the lift coefficient are also visible in the pressure coefficient plot shown in Fig. 4.13. The simulated pressure coefficient on the lower side of the airfoil matches

the experimentally found one for both presented angles of attack. However, the simulation gives smaller pressure coefficients on the upper side compared to the experimental data at 6° angle of attack. This goes along with a higher airfoil lift, and confirms the findings presented in Fig. 4.12. Fig. 4.14 shows the drag polar of the FX05-188 at two different Reynolds numbers. Again, novel simulation approach and measurement coincide at moderate lift conditions but deviate with higher lift. Reynolds number effects on total airfoil drag are evident and can be captured with the novel approach.

4.4. NASA NLF 10-15

The NASA Natural Laminar Flow 10-15 airfoil (see Fig. 4.15) was designed for high-altitude long-endurance unmanned aircraft and investigated in [33, 37].



Fig. 4.15 NLF 10-15 airfoil, max t/c=15.0%, max. camber=4.3%

Airfoil lift and moment simulated with the novel approach are in agreement with wind tunnel data presented in Fig. 4.16. Maximum lift is over predicted, by about 6%. An additional XFOIL simulation (N=9) shows a similar level of accuracy with even a better prediction of the lift coefficient at high angles of attack.

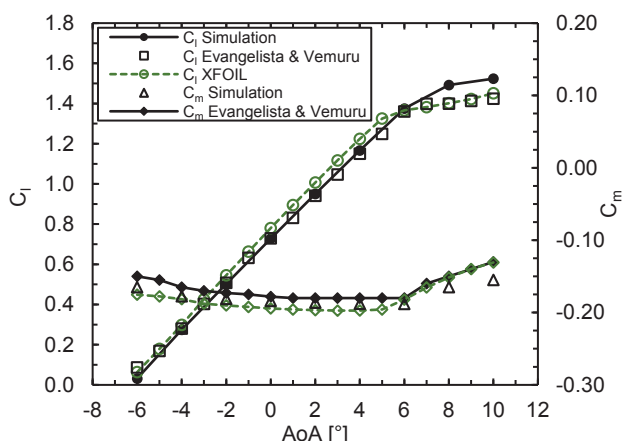


Fig. 4.16 Lift and moment coefficient of NLF 10-15 airfoil at Re=1,000,000 with experimental data from [33]

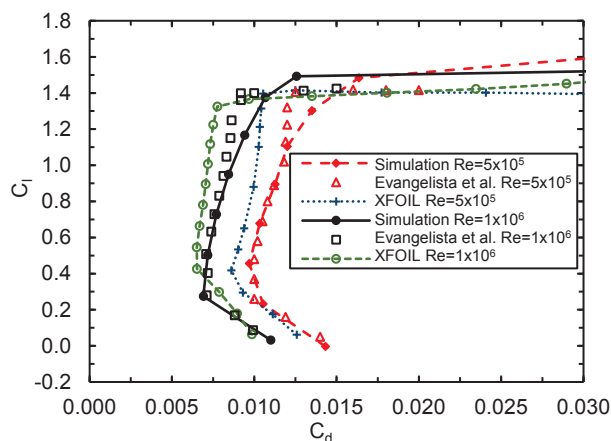


Fig. 4.17 Drag polar of NLF 10-15 airfoil with experimental data from [33]

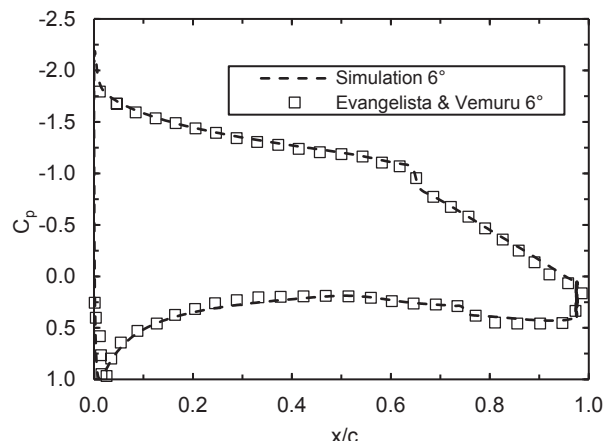


Fig. 4.18 Pressure coefficient of NLF 10-15 at Re=1,000,000 with experimental data from [33]

The airfoil's drag polar is presented in Fig. 4.17, together with wind tunnel data and XFOIL simulations. The novel approach gives close results compared to wind tunnel data at both presented Reynolds numbers for moderate lift (drag deviations <5%). At high lift conditions, simulated drag is higher than measured in the wind tunnel. The XFOIL simulation again shows a too small drag, over a wide range of moderate lift coefficients. However, the course of the drag polar qualitatively matches wind tunnel data.

4.5. NACA 0015

The NACA 0015 is a basic symmetric airfoil shape often used for tail sections. It was investigated several times (e.g. [34, 38]) in various wind tunnels.

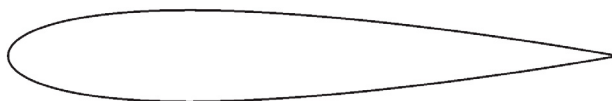


Fig. 4.19 NACA 0015 airfoil, max. $t/c=15\%$, max. camber=0%

Lift and moment coefficient of the airfoil simulated with the novel procedure are compared to wind tunnel measurements and XFOIL computations (N=9) in Fig. 4.20. The novel approach captures the lift characteristics up to stall

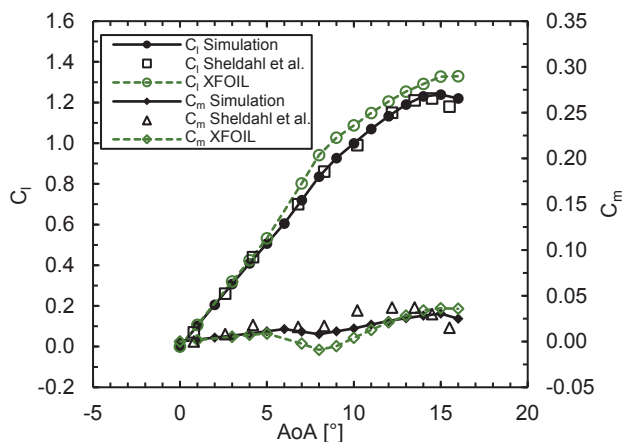


Fig. 4.20 Lift and moment coefficient of NACA 0015 airfoil at $Re=680,000$ with experimental data from [34]

The novel simulation approach shows superior accuracy for simulating airfoil drag compared to XFOIL. An exemplary plot of the pressure coefficient on the airfoil's surface is given in Fig. 4.18. The simulation is able to accurately capture the jump in pressure associated with boundary layer transition (upper surface $x/c=0.65$, lower surface $x/c=0.77$) and the general behavior of the pressure coefficient.

conditions. XFOIL shows a non-linear lift curve slope already in moderate lift conditions and too high lift values above 7° angle of attack.

The simulated moment coefficient gives a trend that agrees to the measurements but with percentage deviations in the order of 50% due to the small absolute values. XFOIL shows a similar trend but with higher deviations to wind tunnel data.

The simulated drag polar of the airfoil is presented in Fig. 4.21 together with experimental results and XFOIL calculations. The novel simulation approach gives results that are very close to experimental ones with slight deviations at high-lift conditions. XFOIL gives good results at moderate lift conditions but shows too small drag values in high-lift conditions.

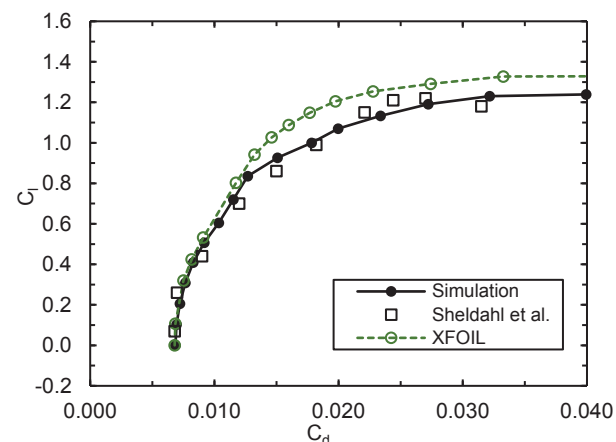


Fig. 4.21 Drag polar of NACA 0015 airfoil at $Re=680,000$ with experimental data from [34]

5. CONCLUSION

The paper presents a novel approach to automate low Reynolds number RANS airfoil simulations with transition effects. The new procedure combines existing software tools in an innovative way and reduces human interacting to specifying airfoil shapes and flow properties.

$\gamma-Re_\theta$ and γ transition model are coupled with the SST turbulence model to predict laminar to turbulent transition also capturing the significant effects of transition bubbles. Both transition models show very similar results.

The application of the novel method is demonstrated by comparing numerical simulations of a wide variety of airfoils with wind tunnel data. The novel procedure is accurate in

simulating lift, drag, moment, and transition behavior for all presented cases. Slight deviations between experiments and simulation are usually restricted to high-lift conditions while very good accuracy is achieved at moderate lift conditions. The novel procedure shows far superior performance for simulating airfoil drag affected by transition bubbles in direct comparison to XFOIL.

The novel method gives engineers and researchers the opportunity to perform large-scale aerodynamic studies with RANS CFD at a level of automation that was previously only achievable with panel methods.

6. ACKNOWLEDGEMENT

The authors like to express their gratitude to Siemens PLM Software for providing academic licenses of their software StarCCM+.

REFERENCES

- [1] Winslow, J., Otsuka, H., Govindarajan, B., and Chopra, I., "Basic Understanding of Airfoil Characteristics at Low Reynolds Numbers (104–105)," *Journal of Aircraft*; Vol. 55, No. 3, 2018, pp. 1050–1061. doi: 10.2514/1.C034415.
- [2] Drela, M., "XFOIL: An Analysis and Design System for Low Reynolds Number Airfoils," *Conference on Low Reynolds Number Airfoil Aerodynamics*, University of Notre Dame, 1989.
- [3] Eppler, R., and Somers, D. M., "A Computer Program for the Design and Analysis of Low-Speed Airfoils: NASA-TM-80210," NASA, Hampton, VA, 1980.
- [4] Selig, M., "Low Reynolds Number Airfoil Design lecture Notes," University of Illinois at Urbana-Champaign, Illinois, 2003.
- [5] Chen, W., and Bernal, L., "Design and Performance of Low Reynolds Number Airfoils for Solar-Powered Flight," *46th AIAA Aerospace Sciences Meeting and Exhibit*, AIAA, Reston, VA, 2008.
- [6] Althaus, D., and Wurz, W., "Wind Tunnel Tests of the SM701 Airfoil and the UAG 88-143/20 Airfoil," *Technical Soaring*; Vol. 17, No. 1, 1993, pp. 21–32.
- [7] Ramanujam, G., Özdemir, H., and Hoeijmakers, H. W. M., "Improving Airfoil Drag Prediction," *Journal of Aircraft*; Vol. 53, No. 6, 2016, pp. 1844–1852. doi: 10.2514/1.C033788.
- [8] Menter, F. R., Langtry, R. B., Likki, S. R., Suzen, Y. B., Huang, P. G., and Völker, S., "A Correlation-Based Transition Model Using Local Variables—Part I: Model Formulation," *Journal of Turbomachinery*; Vol. 128, No. 3, 2006, p. 413. doi: 10.1115/1.2184352.
- [9] Menter, F. R., Smirnov, P. E., Liu, T., and Avancha, R., "A One-Equation Local Correlation-Based Transition Model," *Flow, Turbulence and Combustion*; Vol. 95, No. 4, 2015, pp. 583–619. doi: 10.1007/s10494-015-9622-4.
- [10] Menter, F. R., "Two-equation eddy-viscosity turbulence models for engineering applications," *AIAA Journal*; Vol. 32, No. 8, 1994, pp. 1598–1605. doi: 10.2514/3.12149.
- [11] Langtry, R. B., Menter, F. R., Likki, S. R., Suzen, Y. B., Huang, P. G., and Völker, S., "A Correlation-Based Transition Model Using Local Variables—Part II: Test Cases and Industrial Applications," *Journal of Turbomachinery*; Vol. 128, No. 3, 2006, p. 423. doi: 10.1115/1.2184353.
- [12] Malan, P., Suluksna, K., and Juntasaro, E., "Calibrating the γ -Re θ Transition Model for Commercial CFD," *47th AIAA Aerospace Sciences Meeting including The New Horizons Forum and Aerospace Exposition*, AIAA, Reston, VA, 2009. doi: 10.2514/6.2009-1142.
- [13] Karasu, I., Genc, S. M., and Acikel, H. H., "Numerical Study on Low Reynolds Number Flows Over an Aerofoil," *Journal of Applied Mechanical Engineering*; Vol. 02, No. 05, 2013. doi: 10.4172/2168-9873.1000131.
- [14] Gloudemans, J., Davis, P., and Gelhausen, P., "A rapid geometry modeler for conceptual aircraft," *34th Aerospace Sciences Meeting and Exhibit*, AIAA, Reston, VA, 1996. doi: 10.2514/6.1996-52.
- [15] Siemens PLM Software, "StarCCM+ Documentation," Siemens PLM, Plano, Texas, 2019.
- [16] Götten, F., Havermann, M., Braun, C., Gómez, F., and Bil, C., "RANS Simulation Validation of a Small Sensor Turret for UAVs," *Journal of Aerospace Engineering*; Vol. 32, No. 5, 2019, p. 4019060. doi: 10.1061/(ASCE)AS.1943-5525.0001055.
- [17] Ren, K., Hu, J., Xiong, X., Zhang, L., and Wei, J., "Validation of Turbulence Models in STAR-CCM+ by N.A.C.A. 23012 Airfoil Characteristics," *ASEE Northeast Section Conference*, edited by ASEE, Bridgeport, 2009.
- [18] CD-adapco, "Validation of Star-CCM+ for External Aerodynamics in the Aerospace Industry," <https://mdx2.plm.automation.siemens.com/presentation/validation-star-ccm-external-aerodynamics-aerospace-industry>, [retrieved 2 August 2019].
- [19] OpenVSP, "OpenVSP Wiki - File formats," <http://openvsp.org/wiki/doku.php?id=files>.
- [20] Rumsey, C., "Turbulence Modeling Resource 2D NACA 0012 Airfoil Validation Case: Effect of Far-field Boundary," https://turbmod-els.larc.nasa.gov/naca0012_val_ffeffect.html, [retrieved 4 June 2019].
- [21] Young, A. D., *Boundary Layers*, AIAA Education Series, Washington, DC, 1989.
- [22] Spalart, P. R., and Rumsey, C. L., "Effective Inflow Conditions for Turbulence Models in Aerodynamic Calculations," *AIAA Journal*; Vol. 45, No. 10, 2007, pp. 2544–2553. doi: 10.2514/1.29373.
- [23] Ladson, C. L., "Effects of independent variation of Mach and Reynolds numbers on the low-speed aerodynamic characteristics of the NACA 0012 airfoil section: NASA-TM-4074," NASA, Hampton, VA, 1988.
- [24] Perić, M., and Ferguson, S., "The advantage of polyhedral meshes," 2005, <https://pdfs.semanticscholar.org/51ae/90047ab44f53849196878bfec4232b291d1c.pdf>.
- [25] Vinokur, M., "On one-dimensional stretching functions for finite-difference calculations," *Journal of Computational Physics*; Vol. 50, No. 2, 1983, pp. 215–234. doi: 10.1016/0021-9991(83)90065-7.

- [26] Schlichting, H., and Gersten, K., *Boundary-Layer Theory*, 9th edn., Springer Berlin Heidelberg, Berlin, Heidelberg, s.l., 2017.
- [27] Götten, F., Havermann, M., Braun, C., Gómez, F., and Bil, C., "On the Applicability of Empirical Drag Estimation Methods for Unmanned Air Vehicle Design," *18th AIAA Aviation Technology Integration and Operations Conference*, AIAA, Reston, VA, 2018. doi: 10.2514/6.2018-3192.
- [28] Menter, F. R., Kuntz, M., and Langtry, R., "Ten Years of Industrial Experience with the SST Turbulence Model," *Turbulence, Heat and Mass Transfer 4: Proceedings of the Fourth International Symposium, Heat and Mass Transfer*, Begell House, Inc, New York, 2003.
- [29] Hellsten, A. K., "New Advanced k-w Turbulence Model for High-Lift Aerodynamics," *AIAA Journal*; Vol. 43, No. 9, 2005, pp. 1857–1869. doi: 10.2514/1.13754.
- [30] Mathur, S. R., and Murthy, J. Y., "A Pressure-Based Method for Unstructured Meshes," *Numerical Heat Transfer, Part B: Fundamentals*; Vol. 31, No. 2, 1997, pp. 195–215. doi: 10.1080/10407799708915105.
- [31] Selig, M., and McGranahan, B., "Wind Tunnel Aerodynamic Tests of Six Airfoils for Use on Small Wind Turbines: National Renewable Energy Laboratory," University of Illinois at Urbana-Champaign, Battelle, 2003.
- [32] Wortmann, F. X., "Experimentelle Untersuchungen an neuen Laminarprofilen für Segelflugzeuge und Hubschrauber: Mitteilung aus dem Institut für Gasströmungen der TH Stuttgart," *Zeitschrift für Flugwissenschaften*; Vol. 5, No. 8, 1957, pp. 228–243.
- [33] Evangelista, R., and Vemuru, C., "Evaluation of an analysis method for low-speed airfoils by comparison with wind tunnel results," *27th Aerospace Sciences Meeting*, AIAA, Reston, 1989.
- [34] Sheldahl, R. E., and Klimas, P. C., "Aerodynamic Characteristics of Seven Symmetrical Airfoil Sections Through 180-Degree Angle of Attack for Use in Aerodynamic Analysis of Vertical Axis Wind Turbines," Sandia National Laboratories, Albuquerque, New Mexico, 1981.
- [35] McGhee, R. J., Walker, B. S., and Millard, B. F., "Experimental Results for the Eppler 387 Airfoil at Low Reynolds Numbers in the Langley Low Turbulence Pressure Tunnel: NACA TM 4062," NASA, Hampton, VA, 1988.
- [36] Nicks, O., Steen, G., Heffner, M., and Bauer, D., "Wind Tunnel Investigation and Analysis of the SM701 Airfoil," *Technical Soaring*; Vol. 16, No. 4, 1992, pp. 109–115.
- [37] Maughmer, M. D., and Somers, D. M., "An airfoil designed for a high-altitude, long endurance remotely piloted vehicle," *5th Applied Aerodynamics Conference*, American Institute of Aeronautics and Astronautics, Reston, Virginia, 1987. doi: 10.2514/6.1987-2554.
- [38] Franck, B., "NACA0015 Measurements in LM Wind Tunnel and Turbulence Generated Noise," Risø National Laboratory for Sustainable Energy - Technical University of Denmark, Roskilde, Denmark, 2008.